Draft version February 24, 2022
Typeset using LaTeX **twocolumn** style in AASTeX631

Schwarzschild and Ledoux are equivalent on evolutionary timescales

Evan H. Anders,[1,2] Adam S. Jermyn,[3,2] Daniel Lecoanet,[1,4,2] Adrian E. Fraser,[5,2] Imogen G. Cresswell,[6,2] Meridith Joyce,[7,2] and J. R. Fuentes[8]

[1] *CIERA, Northwestern University, Evanston IL 60201, USA*
[2] *Kavli Institute for Theoretical Physics, University of California, Santa Barbara, CA 93106, USA*
[3] *Center for Computational Astrophysics, Flatiron Institute, New York, NY 10010, USA*
[4] *Department of Engineering Sciences and Applied Mathematics, Northwestern University, Evanston IL 60208, USA*
[5] *Department of Applied Mathematics, Baskin School of Engineering, University of California, Santa Cruz, CA 95064, USA*
[6] *Department Astrophysical and Planetary Sciences & LASP, University of Colorado, Boulder, CO 80309, USA*
[7] *Space Telescope Science Institute, 3700 San Martin Drive, Baltimore, MD 21218, USA*
[8] *Department of Physics and McGill Space Institute, McGill University, 3600 rue University, Montreal, QC H3A 2T8, Canada*

(Received; Revised; Accepted; Published)

Submitted to ApJ

ABSTRACT

In one-dimensional stellar evolution models, convective boundaries are calculated using either the Schwarzschild or Ledoux criterion, but there remains confusion regarding which criterion to use. In this letter, we present a 3D hydrodynamical simulation of a convection zone and adjacent radiative zone, including both thermal and compositional buoyancy forces. As expected, regions which are unstable according to the Ledoux criterion are convective. Initially, the radiative zone adjacent to the convection zone is Schwarzschild-unstable but Ledoux-stable due to a composition gradient. Over many convective overturn timescales the convection zone grows via entrainment. The convection zone saturates at the size predicted by the Schwarzchild criterion, and in this final state the Schwarzschild and Ledoux criteria are equivalent. Therefore, the size of stellar convection zones is determined by the Schwarzschild criterion, except possibly during short-lived stages in which entrainment persists.

Keywords: Stellar convection zones (301), Stellar physics (1621); Stellar evolutionary models (2046)

1. INTRODUCTION

The treatment of convective boundaries in stars is a long-standing problem in modern astrophysics. There are discrepancies between models and observations regarding the sizes of convective cores (Claret & Torres 2018; Joyce & Chaboyer 2018; Viani & Basu 2020; Pedersen et al. 2021; Johnston 2021), the depth of convective envelopes in solar-type stars (inferred from lithium abundances; Pinsonneault 1997; Sestito & Randich 2005; Carlos et al. 2019; Dumont et al. 2021), and the sound speed at the base of the Sun's convection zone (see Basu 2016, Sec. 7.2.1). Incorrect convective boundary locations can have important impacts across astrophysics such as affecting the mass of stellar remnants (Farmer et al. 2019; Mehta et al. 2022) and the inferred radii of exoplanets (Basu et al. 2012; Morrell 2020).

While convective boundary mixing (CBM) has many uncertainties, the most fundamental question is: what determines the location of convection zone boundaries? Some stellar evolution models determine the location of the convection zone boundary using the *Schwarzschild criterion*, by comparing the radiative and adiabatic temperature gradients. In other models, the convection zone boundary is determined by using the *Ledoux criterion*, which also accounts for compositional stratification (Salaris & Cassisi 2017, chapter 3, reviews these criteria). Recent work states that these criteria should predict the same convective boundary location (Gabriel et al. 2014; Paxton et al. 2018, 2019), but in practice these criteria often provide distinct convective bound-

Corresponding author: Evan H. Anders
evan.anders@northwestern.edu

ary locations in stellar evolution software instruments, and this has led to a variety of algorithms for determining boundary locations (Paxton et al. 2018, 2019).

Due to disagreement regarding which stability criterion to implement in 1D models (see Kaiser et al. 2020, chapter 2), and additional confusion regarding even *how* to properly implement them, insight can be gained from studying multi-dimensional simulations. Such simulations show that a convection zone adjacent to a Ledoux-stable region can expand by entraining material from the stable region (Meakin & Arnett 2007; Woodward et al. 2015; Jones et al. 2017; Cristini et al. 2019; Fuentes & Cumming 2020; Andrassy et al. 2020, 2021). However, past simulations have not achieved a statistically-stationary state, leading to uncertainty in how to include entrainment in 1D models (Staritsin 2013; Scott et al. 2021).

In this letter, we present a 3D hydrodynamical simulation that demonstrates that convection zones adjacent to regions that are Ledoux-stable but Schwarzschild-unstable will entrain material until the adjacent region is stable by both criteria. Therefore, in 1D stellar evolution models, the Schwarzschild criterion correctly determines the location of the convective boundary when evolutionary timescales are much larger than the convective overturn timescale (e.g., on the main sequence; Georgy et al. 2021). When correctly implemented, the Ledoux criterion should return the same result (Gabriel et al. 2014). We discuss these criteria in Sec. 2, describe our simulation in Sec. 3, and briefly discuss the implications of our results for 1D stellar evolution models in Sec. 4.

2. THEORY & EXPERIMENT

The Schwarzschild criterion for convective stability is

$$\mathcal{Y}_\mathrm{S} \equiv \nabla_\mathrm{rad} - \nabla_\mathrm{ad} < 0, \tag{1}$$

whereas the Ledoux criterion for convective stability is

$$\mathcal{Y}_\mathrm{L} \equiv \mathcal{Y}_\mathrm{S} + \frac{\chi_\mu}{\chi_T}\nabla_\mu < 0. \tag{2}$$

The temperature gradient $\nabla \equiv d\ln P/d\ln T$ (pressure P and temperature T) is ∇_ad for an adiabatic stratification and ∇_rad if the flux is entirely carried radiatively. The Ledoux criterion includes the effects of the composition gradient $\nabla_\mu = d\ln\mu/d\ln P$ (mean molecular weight μ), where $\chi_T = (d\ln P/d\ln T)_{\rho,\mu}$ and $\chi_\mu = (d\ln P/d\ln \mu)_{\rho,T}$ (density ρ).

Stellar structure software instruments assume that the location of convective boundaries coincide with sign changes of $\mathcal{Y}_\mathrm{L}$ or $\mathcal{Y}_\mathrm{S}$ (Paxton et al. 2018, sec. 2). The various stability regimes that can occur in stars are described in section 3 and figure 3 of Salaris & Cassisi (2017), but we note four important regimes here:

1. Convection Zones (CZs): Regions with both $\mathcal{Y}_\mathrm{S} > 0$ and $\mathcal{Y}_\mathrm{L} > 0$ are convectively unstable.
2. Radiative Zones (RZs): Regions with $\mathcal{Y}_\mathrm{S} < 0$ and $\mathcal{Y}_\mathrm{L} \leq \mathcal{Y}_\mathrm{S}$ are always stable to convection. Other combinations of $\mathcal{Y}_\mathrm{L}$ and $\mathcal{Y}_\mathrm{S}$ may also be RZs, as detailed below in #3 and #4.
3. "Semiconvection" Zones (SZs): Regions with $\mathcal{Y}_\mathrm{S} > 0$ but $\mathcal{Y}_\mathrm{L} < 0$ are stablized to convection by a composition gradient despite an unstable thermal stratification. These regions can be stable RZs or linearly unstable to oscillatory double-diffusive convection (ODDC, see Garaud 2018, chapters 2 and 4).
4. "Thermohaline" Zones: Regions with $\mathcal{Y}_\mathrm{S} < 0$ and $\mathcal{Y}_\mathrm{L} > \mathcal{Y}_\mathrm{S}$ are thermally stable to convection despite an unstable composition gradient. These regions can be stable RZs or linearly unstable to thermohaline mixing (see Garaud 2018, chapters 2 and 3).

In this letter, we study a three-layer 3D simulation of convection. The initial structure of the simulation is an unstable CZ (bottom, #1), a compositionally-stabilized SZ (middle, #3), and a thermally stable RZ (top, #2). We examine how the boundary of the CZ evolves through entrainment. In particular, we are interested in determining whether the heights at which $\mathcal{Y}_\mathrm{S} = 0$ and $\mathcal{Y}_\mathrm{L} = 0$ coincide on timescales that are long compared to the dynamical timescale but short compared to evolutionary timescales.

In this work, we utilize a 3D model employing the Boussinesq approximation, which is formally valid when motions occur on length scales much smaller than the pressure scale height. This approximation fully captures the primary focus of this work, which is nonlinear advective mixing near the CZ-SZ boundary. While the length scales in our simulation are formally much smaller than a scale height, it may be helpful to think of the convection zone length scale ($\sim 1-2$ height units in our simulations) to be analogous to the mixing length in stellar evolution software instruments. Our simulations use a height-dependent ∇_rad and buoyancy is determined by a combination of the composition and the temperature stratification, so $\mathcal{Y}_\mathrm{S}$ and $\mathcal{Y}_\mathrm{L}$ are determined independently and self-consistently. For details on our model setup and Dedalus (Burns et al. 2020) simulations, we refer the reader to appendices A and B.

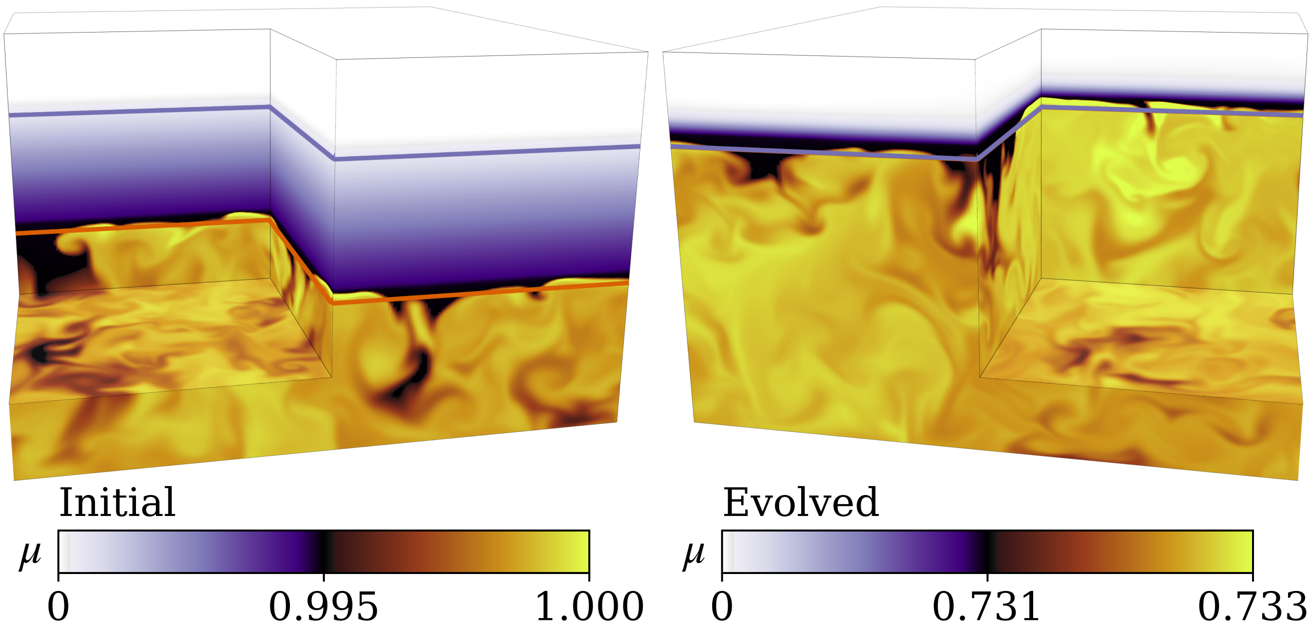

Figure 1. Volume renderings of the composition μ at early (left) and late (right) times. The change in color from white at the top of the box to dark purple at the top of the convection zone denotes a stable composition gradient. The convection zone is well-mixed, so we expand the colorbar scaling there; black represents entrained low-μ fluid being mixed into the yellow high-μ convection zone. The orange and purple horizontal lines respectively denote the heights at which $\mathcal{Y}_\mathrm{L} = 0$ and $\mathcal{Y}_\mathrm{S} = 0$. The two criteria are equivalent in the right panel, so the orange line is not visible. The simulation domain spans $z \in [0, 3]$, but we only plot $z \in [0, 2.5]$ here.

3. RESULTS

In Fig. 1, we visualize the composition field in our simulation near the initial state (left) and evolved state (right). Overplotted horizontal lines correspond to the convective boundaries via the Ledoux (orange, $\mathcal{Y}_\mathrm{L} = 0$) and Schwarzschild (purple, $\mathcal{Y}_\mathrm{S} = 0$) criteria. Initially, the bottom third of the domain is a CZ, the middle third is an SZ, and the top third is an RZ. Convection motions extend beyond $\mathcal{Y}_\mathrm{L} = 0$ at all times; we refer to these motions as overshoot (which is discussed in Korre et al. 2019). Overshoot occurs because the Ledoux boundary is not the location where convective velocity is zero, but rather the location where buoyant acceleration changes sign due to a sign change in the entropy gradient.

The most obvious change from the left to the right panel is that the CZ has consumed the SZ and fills the bottom two-thirds of the box. Overshooting convective motions entrain low-composition material into the CZ where it is homogenized. This process increases the size of the CZ and repeats over thousands of convective overturn times until the Ledoux and Schwarzschild criteria predict the same convective boundary. After this "entrainment" phase, the convective boundary stops moving. The boundary is stable because the radiative flux renews and reinforces the stable temperature gradient; there is no analogous process to reinforce the composition gradient[1].

Figure 2 displays vertical simulation profiles in the initial (left) and evolved (right) states. Shown are the composition μ (top), the discriminants $\mathcal{Y}_\mathrm{L}$ and $\mathcal{Y}_\mathrm{S}$ (middle), and the square Brunt–Väisälä frequency (bottom) as well as the square convective frequency defined as

$$f^2_\mathrm{conv} = \frac{|\mathbf{u}|^2}{\ell^2_\mathrm{conv}}, \tag{3}$$

where $|\mathbf{u}|$ is the horizontally-averaged velocity magnitude and ℓ_conv is the depth of the convectively unstable layer.

Initially, the composition is uniform in the CZ ($z < 1$) and RZ ($z > 2$), but varies linearly in the SZ ($z \in [1, 2]$). We have $\mathcal{Y}_\mathrm{L}(z = 1) \approx 0$ but $\mathcal{Y}_\mathrm{S}(z = 3) \approx 0$. The Brunt–Väisälä frequency N^2 is negative in a boundary layer at the base of the CZ which drives the instability. N^2 is stable for $z \gtrsim 1$, and is larger in the RZ than the SZ by an order of magnitude. We found similar results in simulations where N^2 was constant across the RZ and SZ.

[1] Nuclear timescales are generally much longer than dynamical timescales and can be neglected as a source of composition.

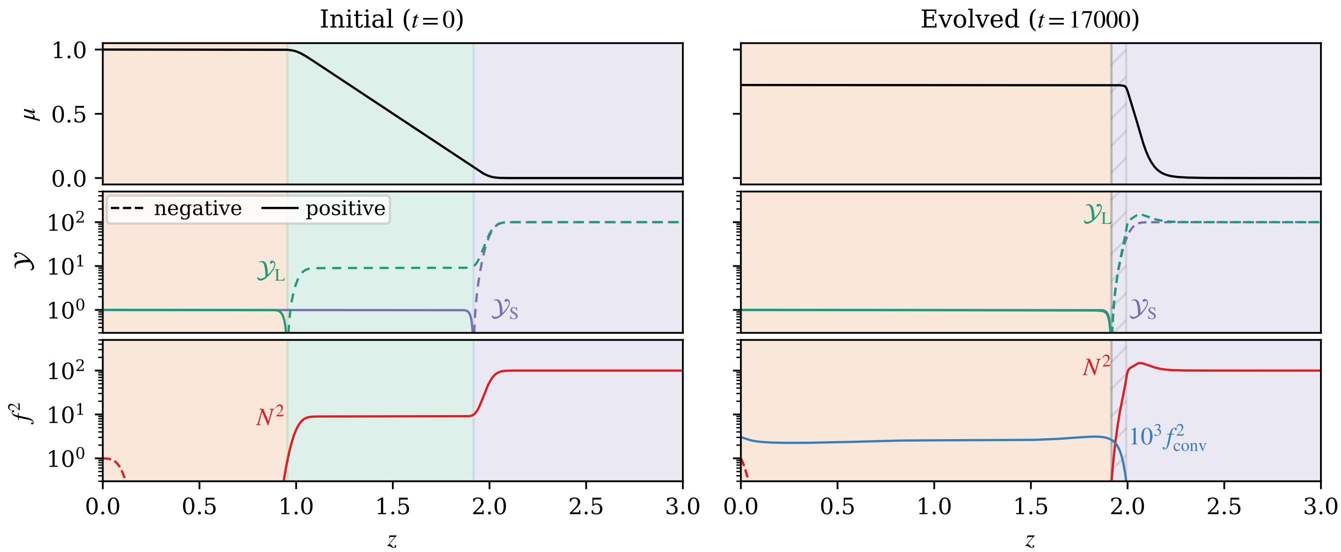

Figure 2. Horizontally-averaged profiles of the composition (top), the discriminants $\mathcal{Y}_\mathrm{S}$ and $\mathcal{Y}_\mathrm{L}$ (middle, Eqns. 1 & 2), and the Brunt–Väisälä frequency $N^2 = -\mathcal{Y}_\mathrm{L}$ and the square convective frequency f^2_conv (bottom, Eqn. 3). Positive and negative values are respectively solid and dashed lines. We show the initial (left) and evolved (right, time-averaged over 100 convective overturn times) states. There are no motions in the initial state, so $f^2_\mathrm{conv} = 0$ and does not appear. The background color is orange in CZs, green in SZs, and purple in RZs per Section 2. The lightly hashed background region in the evolved RZ is the mechanical overshoot zone.

In the evolved state (right panels), the composition profile (top) is constant in the CZ and overshoot zone (denoted as a transparent hashed region), but decreases abruptly at the top of the overshoot zone. The top of the hashed overshoot zone is taken to be the height where the horizontally-averaged kinetic energy falls below 10% of its bulk-CZ value. The Schwarzschild and Ledoux criteria agree upon the location of the convective boundary (middle).

Furthermore, in the CZ, the convective frequency is roughly constant and $N^2 \lesssim 0$ (bottom). In the RZ, $f^2_\mathrm{conv} \approx 0$ and $N^2 \gg 0$. We can compute the "stiffness" of the radiative-convective interface,

$$\mathcal{S} = \frac{N^2|_\mathrm{RZ}}{f^2_\mathrm{conv}|_\mathrm{CZ}}, \tag{4}$$

which is related to the Richardson number $\mathrm{Ri} = \sqrt{\mathcal{S}}$. Convective boundaries in stars often have $\mathcal{S} \gtrsim 10^6$. The time to entrain the SZ is roughly $\tau_\mathrm{entrain} \sim (\delta h/\ell_\mathrm{c})^2 \mathrm{R}_\rho^{-1} \mathcal{S} \tau_\mathrm{dyn}$ (per Fuentes & Cumming 2020, eqn. 3), where δh is the depth of the SZ, ℓ_c is the characteristic convective length scale, $\mathrm{R}_\rho \in [0, 1]$ is the density ratio (see Garaud 2018, eqn. 7), and τ_dyn is the dynamical timescale which is equal to the convective overturn timescale. Our simulation has $\mathcal{S} \sim 10^4$ in the entrainment phase, so it is in the same high-$\mathcal{S}$ regime as stars. We set $\mathrm{R}_\rho = 1/10$. Since the relevant timescale of evolution on the main sequence is the nuclear time τ_nuc, and since $\tau_\mathrm{nuc}/\tau_\mathrm{dyn} \gg (\delta h/\ell_\mathrm{c})^2 \mathcal{S}/\mathrm{R}_\rho$ even for $\mathcal{S} \sim 10^6$, we expect CZs to entrain SZs during a typical stellar evolution timescale for any stage of evolution where convection reaches a steady state. Note also that the low values of R_ρ present in SZs in stars can lead to additional instabilities; we briefly discuss this in Sec. 4.

Finally, Figure 3 displays a Kippenhahn-like diagram of the simulation's evolution. This diagram demonstrates the evolution of the vertical extents of different dynamical regions. The convective boundary measurements are shown as orange ($\mathcal{Y}_\mathrm{L} = 0$) and purple ($\mathcal{Y}_\mathrm{S} = 0$) lines. The CZ is colored orange and fills the region below the Ledoux boundary, the RZ is colored purple and fills the region above the Schwarzschild boundary, and the SZ is colored green and fills the region between these boundaries. Convection motions overshoot above the Ledoux boundary; the hashed zone corresponds to the same overshoot extent displayed in Fig. 2. The *top* of the overshoot zone, denoted by a black line, roughly correspond with the maximum of $\partial\mu/\partial z$ (Fig. 2, upper right), so this describes overshoot well. While the Schwarzschild and Ledoux boundaries start at different heights, 3D convective mixing causes them to converge on dynamical timescales.

4. CONCLUSIONS & DISCUSSION

In this letter, we present a 3D simulation of a convection zone adjacent to a compositionally stable and weakly thermally unstable region. This region is stable

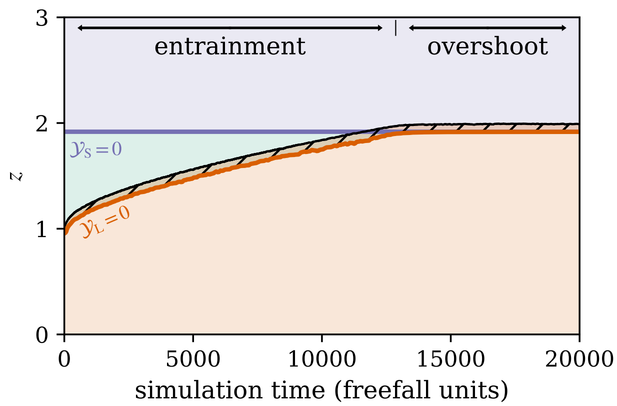

Figure 3. A Kippenhahn-like diagram of the simulation evolution. The y-axis is simulation height and the x-axis is simulation time. The orange line denotes the convective boundary according to the Ledoux criterion ($\mathcal{Y}_{\rm L} = 0$); the CZ is below this and is colored orange. The purple line denotes the convective boundary according to the Schwarzschild criterion ($\mathcal{Y}_{\rm S} = 0$); the RZ is above this and is colored purple. The semiconvective region between these boundaries is colored green. The overshoot zone is hashed, and the black line denotes the top of this region. The simulation has an "entrainment phase" while the CZ expands, and a pure "overshoot phase" where the convective boundary does not advance.

according to the Ledoux criterion, but unstable according to the Schwarzschild criterion. Overshooting convective motions entrain the entire Schwarzschild-unstable region until the Schwarzschild and Ledoux criteria both predict the same boundary of the convection zone.

This simulation demonstrates that, while the Ledoux criterion *instantaneously* predicts the location of the convective boundary, on evolutionary timescales the convective boundary is given by the Schwarzschild criterion (for $t_{\rm evol} \gg (\delta h/\ell_{\rm c})^2 {\rm R}_\rho^{-1} \mathcal{S} t_{\rm dyn}$, see Sec. 3). Our 3D simulation supports the claim that logically consistent implementations of mixing length theory (Gabriel et al. 2014; Paxton et al. 2018, 2019) should have convective boundaries which are Schwarzschild-stable. E.g., the MESA software instrument's "convective pre-mixing" (CPM, Paxton et al. 2019) is consistent with our simulation. Given our results, the predictions made by 1D stellar evolution calculations should not depend on the choice of stability criterion used if/when convective boundary treatments are properly implemented and $t_{\rm evol} \gg (\delta h/\ell_{\rm c})^2 {\rm R}_\rho^{-1} \mathcal{S} t_{\rm dyn}$.

In stars, SZs should be often be unstable to oscillatory double-diffusive convection (ODDC). Mirouh et al. (2012) show that convective layers often emerge from ODDC, and thus mix composition gradients more rapidly than entrainment alone; ODDC is discussed thoroughly in Garaud (2018). Moore & Garaud (2016) apply ODDC to the regions outside core convection zones in main sequence stars, and their results suggest that ODDC formulations should be widely included in stellar models. Despite that, our simulation results demonstrate that entrainment should prevent ODDC-unstable SZs from forming at convective boundaries.

For stages in stellar evolution where $t_{\rm evol} \sim (\delta h/\ell_{\rm c})^2 {\rm R}_\rho^{-1} \mathcal{S} t_{\rm dyn}$, implementations of time-dependent convection (TDC, Kuhfuss 1986) are required to better capture convective dynamics. These evolutionary stages should also implement time-dependent entrainment models to properly advance convective boundaries (e.g., Turner 1968; Fuentes & Cumming 2020).

Anders et al. (2022a) showed convective motions can extend significantly into the radiative zones of stars via "penetrative convection." In this work, we used parameters which do not have significant penetration. This can be seen in the right panels of Fig. 2, because the composition is well-mixed above the convective boundary, but the thermal structure is not.

We assume that the radiative conductivity and $\nabla_{\rm rad}$ do not depend on μ for simplicity. The nonlinear feedback between these effects should be studied in future work, but we expect that our conclusions are robust.

In summary, we find that the Ledoux criterion provides the instantaneous location of the convective boundary, and the Schwarzschild criterion provides the location of the convective boundary in a statistically stationary state; in this final state, the Ledoux and Schwarzschild criteria agree.

We thank Anne Thoul, Dominic Bowman, Jared Goldberg, Tim Cunningham, Falk Herwig, and Kyle Augustson for useful discussions which helped improve our understanding. EHA is funded as a CIERA Postdoctoral fellow and would like to thank CIERA and Northwestern University. The Flatiron Institute is supported by the Simons Foundation. DL and IGC are supported in part by NASA HTMS grant 80NSSC20K1280. AEF acknowledges support from NSF Grant Nos. AST-1814327 and AST-1908338. IGC acknowledges the support of the University of Colorado's George Ellery Hale Graduate Student Fellowship. MJ acknowledges support from the Barry M. Lasker Data Science Fellowship awarded by the Space Telescope Science Institute. JRF acknowledges support from a McGill Space Institute (MSI) Fellowship. This research was supported in part by the National Science Foundation under Grant No. PHY-1748958, and we acknowledge the hospitality of KITP during the Probes of Transport in Stars Program. Computations were conducted with support from the NASA High End Computing (HEC) Program through the NASA Advanced Supercomputing (NAS) Division at Ames Research Center on Pleiades with allocation GID s2276.

APPENDIX

A. MODEL & INITIAL CONDITIONS

In this work we study incompressible, Boussinesq convection with both temperature T and concentration μ. These equations are

$$\nabla\cdot\mathbf{u} = 0 \tag{A1}$$

$$\partial_t\mathbf{u} + \mathbf{u}\cdot\nabla\mathbf{u} + \nabla\varpi = \left(T - \frac{\mu}{\mathrm{R}_\rho}\right)\hat{z} + \frac{\mathrm{Pr}}{\mathrm{Pe}}\nabla^2\mathbf{u}, \tag{A2}$$

$$\partial_t T + \mathbf{u}\cdot(\nabla T - \hat{z}\,\partial_z T_{\mathrm{ad}}) = \nabla\cdot[\kappa_{T,0}\nabla\overline{T}] + \frac{1}{\mathrm{Pe}}\nabla^2 T', \tag{A3}$$

$$\partial_t\mu + \mathbf{u}\cdot\nabla\mu = \frac{\tau_0}{\mathrm{Pe}}\nabla^2\overline{\mu} + \frac{\tau}{\mathrm{Pe}}\nabla^2\mu', \tag{A4}$$

where $\mathbf{u}$ is velocity. Overbars denote horizontal averages and primes denote fluctuations around that average such that $T = \overline{T} + T'$. The adiabatic temperature gradient is $\partial_z T_{\mathrm{ad}}$ and the nondimensional control parameters are

$$\mathrm{Pe} = \frac{\mathrm{u_{ff} h_{conv}}}{\kappa_\mathrm{T}}, \qquad \mathrm{R}_\rho = \frac{|\alpha|\Delta\mathrm{T}}{|\beta|\Delta\mu}, \qquad \mathrm{Pr} = \frac{\nu}{\kappa_T}, \qquad \tau = \frac{\kappa_\mu}{\kappa_T}, \tag{A5}$$

where the nondimensional freefall velocity is $\mathbf{u}_{\mathrm{ff}} = \sqrt{|\alpha| g h_{\mathrm{conv}}\Delta T}$ (with gravitational acceleration g), h_{conv} is the initial depth of the convection zone, $\Delta\mu$ is the composition change across the Ledoux stable region, $\Delta T = h_{\mathrm{conv}}(\partial_z T_{\mathrm{rad}} - \partial_z T_{\mathrm{ad}})$ is the superadiabatic temperature scale of the convection zone, α and β are the coefficients of expansion for T and μ, ν is the viscosity, κ_T is the thermal diffusivity, and κ_μ is the compositional diffusivity. Eqns. A1-A4 are identical to Eqns. 2-5 in Garaud (2018), except we modify the diffusion coefficients acting on $\overline{T}$ ($\kappa_{T,0}$) and $\overline{\mu}$ (τ_0). By doing this, we keep the turbulence (Pe) uniform throughout the domain while also allowing the radiative temperature gradient $\partial_z T_{\mathrm{rad}} = -\mathrm{Flux}/\kappa_{\mathrm{T},0}$ to vary with height. We furthermore reduce diffusion on $\overline{\mu}$ to ensure its evolution is due to advection.

We define the Ledoux and Schwarzschild discriminants

$$\mathcal{Y}_\mathrm{S} = \left(\frac{\partial T}{\partial z}\right)_{\mathrm{rad}} - \left(\frac{\partial T}{\partial z}\right)_{\mathrm{ad}}, \quad \mathcal{Y}_\mathrm{L} = \mathcal{Y}_\mathrm{S} - \mathrm{R}_\rho^{-1}\frac{\partial\mu}{\partial z}, \tag{A6}$$

and in this nondimensional system the square Brunt–Väisälä frequency is the negative of the Ledoux discriminant $N^2 = -\mathcal{Y}_\mathrm{L}$.

We study a three-layer model with $z \in [0, 3]$,

$$\left(\frac{\partial T}{\partial z}\right)_{\rm rad} = \left(\frac{\partial T}{\partial z}\right)_{\rm ad} + \begin{cases} -1 & z \leq 2 \\ 10\mathrm{R}_\rho^{-1} & z > 2 \end{cases}, \tag{A7}$$

$$\frac{\partial \mu_0}{\partial z} = \begin{cases} 0 & z \leq 1 \\ -1 & 1 < z \leq 2 \\ 0 & 2 > z \end{cases}, \tag{A8}$$

We set $\mu = 1$ at $z = 0$ and $T = 1$ at $z = 3$. The intial temperature profile has $\partial_z T_0 = \partial_z T_{\rm rad}$ everywhere except between $z = [0.1, 1]$ where $\partial_z T_0 = \partial_z T_{\rm ad}$. We set $(\partial T/\partial z)_{\rm ad} = -1 - 10\mathrm{R}_\rho^{-1}$. To obtain μ_0, we numerically integrate Eqn. A8 with $\mu_0(z = 0) = 0$. To obtain T_0, we numerically integrate $\partial_z T_0 = (\partial_z T)_{\rm rad}$ (Eqn. A7) with $T_0(z = 3) = 1$.

For boundary conditions, we hold $\partial_z T = \partial_z T_0$ at $z = 0$, $T = T_0$ at $z = 3$, and we set $\partial_z \mu = \hat{z}\cdot\mathbf{u} = \hat{x}\cdot\partial_z\mathbf{u} = \hat{y}\cdot\partial_z\mathbf{u}(z = 0) = \hat{y}\cdot\partial_z\mathbf{u}(z = 3) = 0$ at $z = [0, 3]$. The simulation in this work uses $\mathrm{Pe} = 3.2\times10^3$, $\mathrm{R}_\rho^{-1} = 10$, $\mathrm{Pr} = \tau = 0.5$, $\tau_0 = 1.5\times10^{-3}$, and $\kappa_{T,0} = \mathrm{Pe}^{-1}[(\partial \mathrm{T}/\partial \mathrm{z})_{\rm rad}|_{\rm z=0}]/(\partial\mathrm{T}/\partial\mathrm{z})_{\rm rad}$

B. SIMULATION DETAILS & DATA AVAILABILITY

We time-evolve equations A1-A4 using the Dedalus pseudospectral solver (Burns et al. 2020, git commit 1339061) using timestepper SBDF2 (Wang & Ruuth 2008) and CFL safety factor 0.3. All variables are represented using a Chebyshev series with 512 terms for $z \in [0, 2.25]$, another Chebyshev series with 64 terms for $z \in [2.25, 3]$, and Fourier series in the periodic x and y directions with 192 terms each. Our domain spans $x \in [0, L_x]$, $y \in [0, L_y]$, and $z \in [0, L_z]$ with $L_x = L_y = 4$ and $L_z = 3$. To avoid aliasing errors, we use the 3/2-dealiasing rule in all directions. To start our simulations, we add random noise temperature perturbations with a magnitude of 10^{-6} to the initial temperature field.

Spectral methods with finite coefficient expansions cannot capture true discontinuities. To approximate discontinuous functions such as Eqns. A7 & A8, we define a smooth Heaviside step function centered at $z = z_0$,

$$H(z; z_0, d_w) = \frac{1}{2}\left(1 + \mathrm{erf}\left[\frac{z - z_0}{d_w}\right]\right). \tag{B9}$$

where erf is the error function and we set $d_w = 0.05$.

We produced figures 2 and 3 using matplotlib (Hunter 2007; Caswell et al. 2021). We produced figure 1 using plotly (Inc. 2015) and matplotlib. All of the Python scripts used to run the simulations in this paper and to create the figures in this paper are publicly available in a git repository (https://github.com/evanhanders/schwarzschild_or_ledoux); these scripts and the data that create the figures are online in a Zenodo repository (Anders et al. 2022b).

REFERENCES

Anders, E. H., Jermyn, A. S., Lecoanet, D., & Brown, B. P. 2022a, ApJ, 926, 169, doi: 10.3847/1538-4357/ac408d

Anders, E. H., Jermyn, A. S., Lecoanet, D., et al. 2022b, Supplemental Materials for "Schwarzschild and Ledoux are equivalent on evolutionary timescales", 1.0, Zenodo, doi: 10.5281/zenodo.6230636

Andrassy, R., Herwig, F., Woodward, P., & Ritter, C. 2020, MNRAS, 491, 972, doi: 10.1093/mnras/stz2952

Andrassy, R., Higl, J., Mao, H., et al. 2021, arXiv e-prints, arXiv:2111.01165. https://arxiv.org/abs/2111.01165

Basu, S. 2016, Living Reviews in Solar Physics, 13, 2, doi: 10.1007/s41116-016-0003-4

Basu, S., Verner, G. A., Chaplin, W. J., & Elsworth, Y. 2012, ApJ, 746, 76, doi: 10.1088/0004-637X/746/1/76

Burns, K. J., Vasil, G. M., Oishi, J. S., Lecoanet, D., & Brown, B. P. 2020, Physical Review Research, 2, 023068, doi: 10.1103/PhysRevResearch.2.023068

Carlos, M., Meléndez, J., Spina, L., et al. 2019, MNRAS, 485, 4052, doi: 10.1093/mnras/stz681

Caswell, T. A., Droettboom, M., Lee, A., et al. 2021, matplotlib/matplotlib: REL: v3.3.4, v3.3.4, Zenodo, doi: 10.5281/zenodo.4475376

Claret, A., & Torres, G. 2018, ApJ, 859, 100, doi: 10.3847/1538-4357/aabd35

Cristini, A., Hirschi, R., Meakin, C., et al. 2019, MNRAS, 484, 4645, doi: 10.1093/mnras/stz312

Dumont, T., Palacios, A., Charbonnel, C., et al. 2021, A&A, 646, A48, doi: 10.1051/0004-6361/202039515

Farmer, R., Renzo, M., de Mink, S. E., Marchant, P., & Justham, S. 2019, ApJ, 887, 53, doi: 10.3847/1538-4357/ab518b

Fuentes, J. R., & Cumming, A. 2020, Physical Review Fluids, 5, 124501, doi: 10.1103/PhysRevFluids.5.124501

Gabriel, M., Noels, A., Montalbán, J., & Miglio, A. 2014, A&A, 569, A63, doi: 10.1051/0004-6361/201423442

Garaud, P. 2018, Annual Review of Fluid Mechanics, 50, 275, doi: 10.1146/annurev-fluid-122316-045234

Georgy, C., Saio, H., & Meynet, G. 2021, A&A, 650, A128, doi: 10.1051/0004-6361/202040105

Hunter, J. D. 2007, Computing in Science and Engineering, 9, 90, doi: 10.1109/MCSE.2007.55

Inc., P. T. 2015, Collaborative data science, Montreal, QC: Plotly Technologies Inc. https://plot.ly

Johnston, C. 2021, A&A, 655, A29, doi: 10.1051/0004-6361/202141080

Jones, S., Andrassy, R., Sandalski, S., et al. 2017, MNRAS, 465, 2991, doi: 10.1093/mnras/stw2783

Joyce, M., & Chaboyer, B. 2018, ApJ, 864, 99, doi: 10.3847/1538-4357/aad464

Kaiser, E. A., Hirschi, R., Arnett, W. D., et al. 2020, MNRAS, 496, 1967, doi: 10.1093/mnras/staa1595

Korre, L., Garaud, P., & Brummell, N. H. 2019, MNRAS, 484, 1220, doi: 10.1093/mnras/stz047

Kuhfuss, R. 1986, A&A, 160, 116

Meakin, C. A., & Arnett, D. 2007, ApJ, 667, 448, doi: 10.1086/520318

Mehta, A. K., Buonanno, A., Gair, J., et al. 2022, ApJ, 924, 39, doi: 10.3847/1538-4357/ac3130

Mirouh, G. M., Garaud, P., Stellmach, S., Traxler, A. L., & Wood, T. S. 2012, ApJ, 750, 61, doi: 10.1088/0004-637X/750/1/61

Moore, K., & Garaud, P. 2016, ApJ, 817, 54, doi: 10.3847/0004-637X/817/1/54

Morrell, S. A. F. 2020, PhD thesis, University of Exeter

Paxton, B., Schwab, J., Bauer, E. B., et al. 2018, ApJS, 234, 34, doi: 10.3847/1538-4365/aaa5a8

Paxton, B., Smolec, R., Schwab, J., et al. 2019, ApJS, 243, 10, doi: 10.3847/1538-4365/ab2241

Pedersen, M. G., Aerts, C., Pápics, P. I., et al. 2021, Nature Astronomy, 5, 715, doi: 10.1038/s41550-021-01351-x

Pinsonneault, M. 1997, ARA&A, 35, 557, doi: 10.1146/annurev.astro.35.1.557

Salaris, M., & Cassisi, S. 2017, Royal Society Open Science, 4, 170192, doi: 10.1098/rsos.170192

Scott, L. J. A., Hirschi, R., Georgy, C., et al. 2021, MNRAS, 503, 4208, doi: 10.1093/mnras/stab752

Sestito, P., & Randich, S. 2005, A&A, 442, 615, doi: 10.1051/0004-6361:20053482

Staritsin, E. I. 2013, Astronomy Reports, 57, 380, doi: 10.1134/S1063772913050089

Turner, J. S. 1968, Journal of Fluid Mechanics, 33, 183, doi: 10.1017/S0022112068002442

Viani, L. S., & Basu, S. 2020, ApJ, 904, 22, doi: 10.3847/1538-4357/abba17

Wang, D., & Ruuth, S. J. 2008, Journal of Computational Mathematics, 26, 838. http://www.jstor.org/stable/43693484

Woodward, P. R., Herwig, F., & Lin, P.-H. 2015, ApJ, 798, 49, doi: 10.1088/0004-637X/798/1/49